

Reassessing the Spin of Second-born Black Holes in Coalescing Binary Black Holes and Its Connection to the $\chi_{\text{eff}} - q$ Correlation

Zi-Yuan Wang¹, Ying Qin¹, Rui-Chong Hu^{2,3}, Yuan-Zhu Wang⁴, Georges Meynet^{5,6}, and Han-Feng Song⁷

¹ Department of Physics, Anhui Normal University, Wuhu, Anhui, 241002, China
e-mail: yingqin@ahnu.edu.cn

² Nevada Center for Astrophysics, University of Nevada, Las Vegas, NV 89154, USA

³ Department of Physics and Astronomy, University of Nevada, Las Vegas, NV 89154, USA

⁴ Institute for Theoretical Physics and Cosmology, Zhejiang University of Technology, Hangzhou, 310032, China

⁵ Département d'Astronomie, Université de Genève, Chemin Pegasi 51, 1290 Versoix, Switzerland

⁶ Gravitational Wave Science Center (GWSC), Université de Genève, 24 quai E. Ansermet, 1211 Geneva, Switzerland

⁷ College of Physics, Guizhou University, Guiyang city, Guizhou Province, 550025, China

September 9, 2025

ABSTRACT

Context. The mass ratio q and effective inspiral spin χ_{eff} of binary black hole mergers in GWTC-4.0 have been reported to display a weaker anti-correlation compared to GWTC-3, a feature whose origin has been explored by several groups. In this work, within the isolated binary evolution framework, we adopt a recently proposed wind prescription for helium stars to systematically investigate the spin of the second-born black hole and its role in shaping this correlation.

Aims. Our first goal is to investigate the main factors shaping the spin of the second-born black hole in a helium star–black hole binary, whether formed via a common-envelope or stable mass-transfer channel, and to explore the potential correlation between the mass ratio q and the effective inspiral spin χ_{eff} .

Methods. Using the stellar and binary evolution code MESA, which includes a recently proposed helium-star wind prescription alongside internal differential rotation and tidal interactions, we investigate how initial conditions and fundamental physical processes shape the spin of the resulting black hole.

Results. We find that the recently proposed wind prescription for helium stars is substantially weaker than the standard Dutch wind scheme, particularly at subsolar metallicity. Using this scheme, we perform detailed binary modeling of a helium star with a black hole companion. Our results show that the spin magnitude of the resulting black hole is insensitive to the helium star's evolutionary stage at the onset of tidal interactions or to the companion mass. Instead, wind mass loss plays the dominant role: more massive helium-star progenitors produce lower-spinning black holes. The initial stellar rotation has only a minor effect, especially under strong tidal coupling, consistent with the common assumption of orbital synchronization. By contrast, the efficiency of angular momentum transport within helium stars can significantly alter the spin magnitude of the resulting black hole.

Conclusions. The expanded sample from the GWTC-4.0 catalog has provided an opportunity to investigate this anti-correlation. Using the derived relation between the mass and spin of the second-born black hole, we find that the properties of most binary black holes in GWTC-4.0—specifically the mass ratio q and effective inspiral spin χ_{eff} —can be reproduced. We further show that the q – χ_{eff} correlation is sensitive to the assumed mass function (e.g., Gaussian and uniform distribution), displaying notable deviations from the POWER-LAW+PEAK model.

Key words. Close binary stars; Black holes; Wolf-Rayet stars; Gravitational waves

1. Introduction

By the end of the third observing run (O3), the LIGO–Virgo–KAGRA (LVK) collaboration (Acernese et al. 2015; Akutsu et al. 2021) had reported a catalog of 69 gravitational-wave (GW) candidates with a false-alarm rate below 1 yr^{-1} , referred to as GWTC-3 (Abbott et al. 2023a). More recently, the LVK collaboration released GWTC-4.0 (The LIGO Scientific Collaboration et al. 2025b), which includes 84 additional binary black hole (BBH) candidates with the same false-alarm threshold. This growing BBH population has enabled more detailed studies of the distributions of black hole mass, spin, and redshift (Roulet et al. 2020; Abbott et al. 2021b), offering valuable insights into the mechanisms that govern binary black hole formation.

In general, the effective inspiral spin has been widely recognized as a potential probe for distinguishing BBH formation channels. Beyond one-dimensional distributions, correlations between key parameters provide crucial insights into BBH formation scenarios. Using BBH events from the second GW transient catalog (GWTC-2) (Abbott et al. 2021a), Callister et al. (2021) first identified an anti-correlation between the mass ratio q and the effective inspiral spin χ_{eff} . Adamcewicz & Thrane (2022) later reinforced this finding through a statistical copula analysis, showing that BBHs in GWTC-2 with unequal component masses tend to have higher χ_{eff} (98.7% credibility). This correlation was further validated with BBH events in GWTC-3 (Abbott et al. 2023b). Using updated GWTC-3 data, Adamcewicz et al. (2023) improved their copula-based framework and found evidence for an anti-correlation between q and χ_{eff} with 99.7% credibility. While preparing this work, we noted that the

BBH sample was expanded with new candidates reported in GWTC-4.0 (The LIGO Scientific Collaboration et al. 2025b). An updated population study by The LIGO Scientific Collaboration et al. (2025a) found that q and χ_{eff} are anti-correlated at 92% credibility.

Various studies have explored the origin of the $q - \chi_{\text{eff}}$ anti-correlation. One plausible explanation is that BBHs assembled in active galactic nucleus (AGN) disks naturally exhibit such a trend (e.g., McKernan et al. 2022; Santini et al. 2023; Cook et al. 2024; Delfavero et al. 2025; Li et al. 2025). In the context of isolated binary evolution, Bavera et al. (2021) showed that, under the assumption of a high common-envelope ejection efficiency, binaries undergoing common-envelope evolution can also reproduce the observed anti-correlation. Zevin & Bavera (2022) found that stable mass transfer leading to mass ratio reversal may similarly account for the trend. Broekgaarden et al. (2022) systematically explored 560 population synthesis models and showed that the more massive BH forms second in $\gtrsim 70\%$ of BBHs observable by the LVK. In addition, Olejak et al. (2024) argued that a combination of common-envelope and stable mass transfer channels provides a good match to the observed correlation, while Banerjee & Olejak (2024) demonstrated that isolated massive binary evolution via the stable mass transfer subchannel can reproduce the key observed features of BBH populations, including their masses, mass ratios, and spins.

In isolated binary evolution, the common-envelope channel has been extensively studied as a pathway to BBH mergers (e.g., Belczynski et al. 2016; Eldridge & Stanway 2016; Stevenson et al. 2017; Qin et al. 2018; Kruckow et al. 2018; Spera et al. 2019; Mapelli et al. 2019; Marchant et al. 2019; Bavera et al. 2020). Within this framework, Qin et al. (2018) showed that the spin of the first-born BH is typically negligible,¹ whereas the second-born BH can span the full range (i.e., from nonspinning to maximally spinning). Its spin is primarily determined by the competition between stellar winds and tidal interactions during the helium-star (He-star) phase (Qin et al. 2018). However, the strength of He-star winds remains uncertain. Recently, Sander & Vink (2020) proposed the first theoretically motivated prescription for mass loss in massive He stars, and Sander et al. (2023) further suggested incorporating a temperature dependence into the mass-loss rate. In parallel, Sciarini et al. (2024) identified inconsistencies in the implementation of dynamical tides relative to the original formulation of Zahn (1977). This issue was corrected and further tested by Qin et al. (2024a), who found that dynamical tides are slightly weaker than previously assumed (see details in Qin et al. 2024a). The combination of this new wind prescription with the revised tidal treatment enables us to investigate the spin of the BH formed from a He star in a close binary system. Moreover, we try to explore the relation between the mass ratio q and the effective inspiral spin χ_{eff} in binaries consisting of a He-star progenitor and a BH companion.

In this work, we employ the stellar and binary evolution code MESA (Paxton et al. 2011, 2013, 2015, 2018, 2019; Jermyn et al. 2023) to investigate the key factors that determine the spin of the second-born BH formed from a He-star progenitor with a BH companion, as well as the relation between the mass ratio q and the effective inspiral spin χ_{eff} . In Sect. 2, we outline the main physical assumptions underlying our detailed binary evolution models and provide a brief introduction to the He-star wind mass loss. We then present our main findings in Sect. 3. Finally, we summarize the conclusions with some discussion in Sect. 4.

¹ See also Fuller & Ma (2019); Belczynski et al. (2020) reported a small but nonzero value, $\chi \sim 0.1$.

2. Methods

2.1. Main physics adopted in this work

We performed detailed binary modeling using the release version mesa-r15140 of the Modules for Experiments in Stellar Astrophysics (MESA) stellar evolution code (Paxton et al. 2011, 2013, 2015, 2018, 2019; Jermyn et al. 2023). Our He star models were constructed following the methodology outlined in recent studies (e.g., Fragos et al. 2023; Lyu et al. 2023; Qin et al. 2024a,b). Throughout this work, we adopted a solar metallicity of $Z_{\odot} = 0.0142$ (Asplund et al. 2009).

We modeled convection using the mixing-length theory (Böhm-Vitense 1958), adopting a mixing-length parameter of $\alpha_{\text{mlt}} = 1.93$. Convective boundaries were determined based on the Ledoux criterion, with a step-overshooting parameter of $\alpha_p = 0.335 H_p$, calibrated to match the observed drop in rotation rates of massive main-sequence stars (Brott et al. 2011), where H_p represents the pressure scale height at the Ledoux boundary. Semiconvection was included in the He star models following Langer et al. (1983), with an efficiency parameter of $\alpha_{\text{sc}} = 1.0$. For nucleosynthesis calculations, we employed the approx21.net reaction network.

We modeled rotational mixing and angular momentum transport as diffusive processes (Heger & Langer 2000), incorporating the effects of the Goldreich–Schubert–Fricke instability, Eddington–Sweet circulations, as well as secular and dynamical shear mixing. The efficiency of diffusive element mixing was set to $f_c = 1/30$, following Chaboyer & Zahn (1992); Heger & Langer (2000). To account for the sensitivity of the μ -gradient to rotationally induced mixing, we mitigated its impact by multiplying $f_{\mu} = 0.05$, as recommended by Heger & Langer (2000).

Additionally, we accounted for rotationally enhanced mass loss following Heger & Langer (1998) and Langer (1998):

$$\dot{M}(\omega) = \dot{M}(0) \left(\frac{1}{1 - \omega/\omega_{\text{crit}}} \right)^{\xi}, \quad (1)$$

where ω is the angular velocity and ω_{crit} is the critical angular velocity at the stellar surface. The latter is given by

$$\omega_{\text{crit}}^2 = (1 - L/L_{\text{Edd}})GM/R^3, \quad (2)$$

where L , M , and R are the stellar luminosity, mass, and radius, respectively, and G is the gravitational constant. The classical Eddington luminosity, L_{Edd} , is defined using the electron-scattering opacity for a fully ionized medium, $\kappa = 0.2(1 + X) \text{ cm}^2 \text{ g}^{-1}$, with $X = 0$ for a hydrogen-free WR star envelope. We adopted an exponent of $\xi = 0.43$ (Langer 1998). Notably, we did not include gravity-darkening effects, as discussed in Maeder & Meynet (2000).

We applied the theory of dynamical tides to He star stars with radiative envelopes, following the framework of Zahn (1977). The synchronization timescale was computed using the prescriptions of Zahn (1977), Hut (1981), and Hurley et al. (2002), while the tidal torque coefficient E_2 was adopted from the updated fitting formula of Qin et al. (2018). Given previous inconsistencies in the implementation of the synchronization timescale (Sciarini et al. 2024), we adopted the corrected version from Qin et al. (2024a). We adopted the Jeans mode mass loss, i.e., the stellar wind removes the specific angular momentum of the mass-losing star. In our binary modeling, we evolved He stars until their central carbon depletion is reached. Furthermore, we adopted a direct collapse scenario for BH formation (assuming no mass and angular momentum loss), implying that newly formed BHs do not experience mass loss or natal kicks (Belczynski et al. 2008).

2.2. He star mass-loss rates

He stars represent the final evolutionary stage prior to BH formation, making their mass loss a key determinant of the resulting BH mass (Woosley et al. 2020). Stellar evolution models have traditionally relied on empirically derived mass-loss prescriptions for He stars. Based on the mass-loss rate of Yoon (2017), Woosley (2019) investigated the evolution of massive He stars. Notably, the recent work by Sander & Vink (2020) introduced the first theoretically grounded mass-loss formulae for massive He stars. Higgins et al. (2021) adopted this prescription to compare with earlier empirical recipes widely used in stellar evolution and population-synthesis modelling. This wind prescription provides a physically motivated description of mass loss, derived from dynamically consistent atmosphere models for He stars by Sander & Vink (2020), namely,

$$\log\left(\frac{\dot{M}_{\text{SV2020}}}{M_{\odot} \text{ yr}^{-1}}\right) = \alpha \log(\log L - \log L_0) + \frac{3}{4} \log \frac{L}{10L_0} + \log \dot{M}_{10}, \quad (3)$$

where

$$\alpha = 0.32 \log \frac{Z_{\text{init}}}{Z_{\odot}} + 1.40, \quad (4)$$

$$\log L_0/L_{\odot} = -0.87 \log \frac{Z_{\text{init}}}{Z_{\odot}} + 5.06, \quad (5)$$

$$\log\left(\frac{\dot{M}_{10}}{M_{\odot} \text{ yr}^{-1}}\right) = -0.75 \log \frac{Z_{\text{init}}}{Z_{\odot}} - 4.06. \quad (6)$$

In the above equations, Z_{init} is the initial metallicity and L_0 represents the asymptotic limit for which there is theoretically zero mass-loss. The exponent α characterizes the curvature of the breakdown, and \dot{M}_{10} denotes the mass-loss rate at $L = 10 L_0$. When $L \leq L_0$, the luminosity is insufficient to support the optically thick winds, leading to the onset of the “breakdown regime”, where the mass loss becomes zero. To account for this, we adopted the wind prescription proposed by Vink (2017) as the lower limit, namely,

$$\log\left(\frac{\dot{M}}{M_{\odot} \text{ yr}^{-1}}\right) = -13.3 + 1.36 \log(L/L_{\odot}) + 0.61 \log(Z_{\text{cur}}/Z_{\odot}), \quad (7)$$

where Z_{cur} is the current metallicity. When considering the temperature dependence, Sander et al. (2023) adjusted the mass loss of the He wind as follows:

$$\log\left(\frac{\dot{M}_{\text{SV2023}}}{M_{\odot} \text{ yr}^{-1}}\right) = \log\left(\frac{\dot{M}_{\text{SV2020}}}{M_{\odot} \text{ yr}^{-1}}\right) - 6 \log\left(\frac{T_{\text{eff,crit}}}{141 \text{ kK}}\right), \quad (8)$$

where $T_{\text{eff,crit}}$ represents the effective temperature at the critical (\approx sonic) point, and the fixed value of 141 kK accurately represents the $T_{\text{eff,crit}}$ (Sander et al. 2023). To incorporate both theoretical and empirical insights, we adopt a hybrid wind model combining the prescriptions of Sander et al. (2023) and Vink (2017), hereafter referred to as SV2023+.

In MESA, the standard mass-loss prescriptions are unified into the Dutch wind scheme, which employs the rates of Vink et al. (2001) for hot, hydrogen-rich stars, de Jager et al. (1988) for cool stars, and Nugis & Lamers (2000) for hot stars that have lost their hydrogen envelopes. For He stars, the Nugis & Lamers (2000) mass-loss prescription is implemented in MESA as

$$\log\left(\frac{\dot{M}_{\text{NL2000}}}{M_{\odot} \text{ yr}^{-1}}\right) = -11.00 + 1.29 \log L + 1.73 \log Y + 0.47 \log Z_{\text{cur}},$$

where Z_{cur} is the current metallicity and Y is the helium abundance.

Using the two wind prescriptions, we evolve single He stars to examine the relation between their initial mass (He ZAMS) and final mass (at central carbon depletion). The initial He-star masses are chosen to span 5–70 M_{\odot} at both solar ($1.0 Z_{\odot}$) and subsolar ($0.1 Z_{\odot}$) metallicities. The results are shown in Figure 1.

At solar metallicity (left panel), He stars with initial masses $M_{\text{He,i}} \gtrsim 20 M_{\odot}$ undergo substantial mass loss under the SV2023+ wind prescription, losing more than half of their initial mass. The NL2000 prescription yields a qualitatively similar correlation between initial and final mass but drives systematically stronger winds for $M_{\text{He,i}} \gtrsim 20 M_{\odot}$, resulting in even greater mass loss in this regime.

At subsolar metallicity ($0.1 Z_{\odot}$, right panel), mass loss is generally weaker. In particular, for He stars with $M_{\text{He,i}} \lesssim 25 M_{\odot}$, the SV2023+ prescription predicts almost negligible wind-driven mass loss.

3. Results

3.1. Second-born BH spin magnitudes in BH-He binaries

A total of 153 confident BBH events with a false-alarm rate below 1 yr^{-1} have been reported in the GWTC-4.0 (The LIGO Scientific Collaboration et al. 2025b). Using the Hubble time as the maximum merger timescale from Peters (1964), we apply Kepler’s third law to estimate the maximum orbital period at birth for each coalescing binary system:

$$P_{\text{orb,max}} [\text{d}] = \frac{1}{24} \left[\frac{t_{\text{merger}}}{9.829 \times 10^6 \text{ yr}} \frac{M_{\text{BH}_1} M_{\text{BH}_2}}{M_{\text{total}}^{1/3}} \right]^{3/8}, \quad (10)$$

where M_{BH_1} and M_{BH_2} are the component BH masses, and M_{total} represents the total system mass, t_{merger} is expressed in years (assuming a circular orbit), and masses are in units of solar mass.

Figure 2 shows the distribution of the component masses and their corresponding maximum orbital periods ($\lesssim 11.0 \text{ d}$) at birth. We find that the maximum orbital period increases with the component masses. This trend reflects the fact that more massive binaries emit gravitational waves more efficiently and therefore inspiral faster at a given separation. Consequently, they can be born in wider orbits and still merge within a Hubble time, whereas less massive binaries must start in tighter orbits to coalesce on the same timescale. Given that the immediate progenitor of a BBH is a close binary consisting of a BH and a He star, and that the He star undergoes substantial wind-driven mass loss, the orbital period of the BH+He system at birth is expected to be much shorter, since the orbit can otherwise be considerably widened by the wind mass loss.

In the context of the isolated binary evolution, after the common envelope or stable mass transfer phase, the binary system—comprising a BH and a He star—continues to evolve in a compact orbit. As demonstrated by Qin et al. (2018), tidal interactions during the subsequent evolutionary phase are critical in determining the final spin of the newly formed BH. The efficiency of tidal spin-up might depend sensitively on the evolutionary stage of the He star at the onset of this interaction. In addition, the initial rotation of the He star and its companion BH mass may also influence the resulting BH spin. Crucially, wind-driven mass loss from the He star, particularly in high-metallicity environments, can substantially reduce the angular momentum

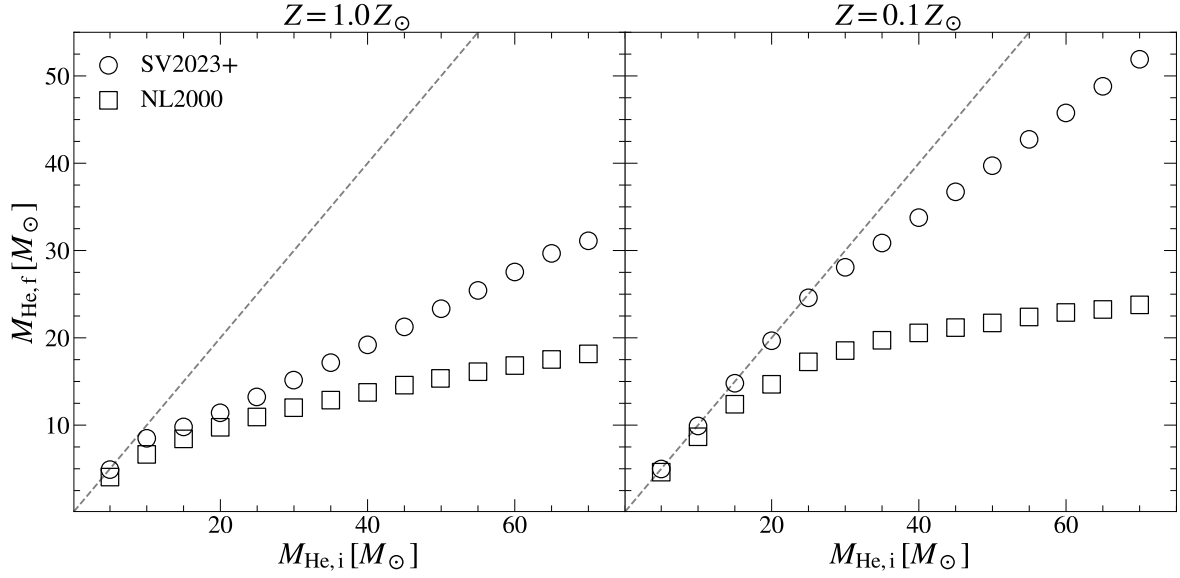


Fig. 1. Final masses of He stars as a function of their initial masses with different wind prescriptions (left panel: $1.0 Z_{\odot}$; right panel: $0.1 Z_{\odot}$). Circle: SV2023+, square: NL2000. The dashed line indicates where the final mass is equal to the initial mass.

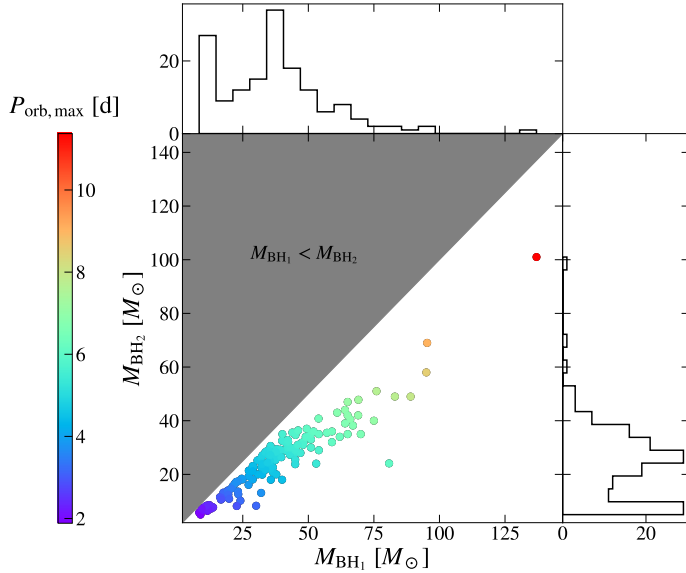


Fig. 2. The maximum initial orbital period of the BBHs, above which the systems would not merge within a Hubble time. Histograms of the primary component masses (upper panel) and the secondary component masses (lower panel).

retained in the collapsing core. In the following sections, we systematically explore these factors, adopting the SV2023+ wind prescription for the He stars at solar metallicity (namely $Z = Z_{\odot}$).

3.1.1. Tidal efficiency on the evolutionary stage of the He star

Tidal interactions between a BH and a He star can affect the angular momentum of the progenitor, potentially influencing the spin of the resulting BH. However, it remains unclear whether the He star has significantly evolved by the time the system forms. To assess whether the spin of the resulting BH can be significantly altered under these conditions, we perform detailed binary evolution modeling for a system comprising a $20 M_{\odot}$ BH

and a $20 M_{\odot}$ He star, exploring initial orbital periods of 0.5, 1.0, and 2.0 d. We examine three different He star models:

- Zero-age helium main sequence (He Zams) star
- He star with 10% of its central helium burned
- He star with 30% of its central helium burned

The He star is assumed to be initially synchronized with the orbit, and we will explore the implications of this assumption in a later section. We also assume that the progenitor star, at the end of its evolution, collapses directly into a BH without losing mass or angular momentum. The synchronization timescale (T_{sync}) represents the time required for tidal interactions to bring the star's spin into sync with the orbital period. We refer readers of interest to the updated formulation provided in Sciarini et al. (2024) and its implementation in Qin et al. (2024a). In the upper panel of Figure 3, we show that T_{sync} evolves as the He star approaches central carbon depletion. During the core-helium burning phase, T_{sync} increases slightly due to orbital widening caused by wind-driven mass loss. After central helium depletion, tidal effects become negligible as the synchronization timescale T_{sync} increases rapidly. This is primarily due to the recession of the convective core, which leads to a significant reduction in the tidal torque coefficient E_2 (see Equation (9) in Qin et al. 2018). In the bottom panel, the spin magnitude χ_2 of the resulting BH gradually decreases but converges to the same value for the three He star models. This result indicates that tidal interactions are highly efficient in close binaries, effectively erasing any differences in spin evolution arising from variations during earlier helium burning.

3.1.2. Tidal efficiency on the initial rotation of He stars

We now investigate how the initial rotation of the He star affects the spin magnitude of the resulting secondary BH. To this end, we perform detailed binary evolution simulations for a system consisting of a $20 M_{\odot}$ BH and a $20 M_{\odot}$ He star in an initial orbit of 1.0 and 0.5 d, considering a range of initial He star spins: $\omega_i = 0$, $\omega_i = 0.3 \omega_{\text{crit}}$, $\omega_i = 0.6 \omega_{\text{crit}}$, $\omega_i = 0.9 \omega_{\text{crit}}$, and synchronized with the orbit. As shown in the upper-left panel of Figure 4,

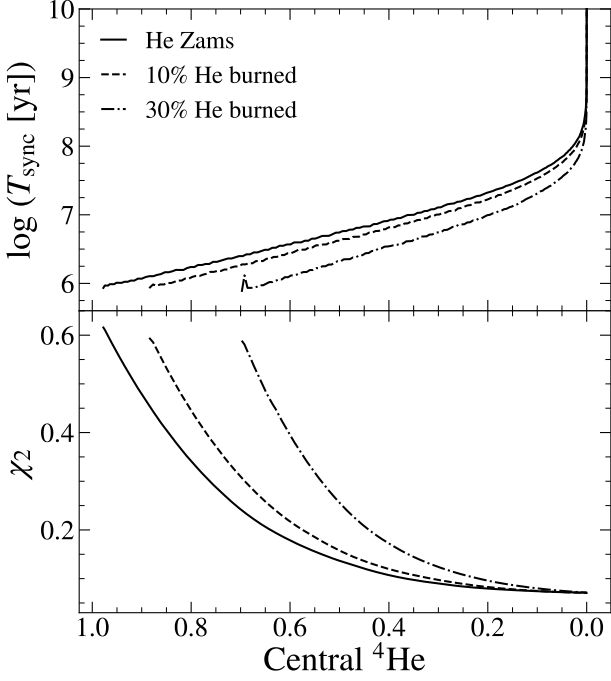


Fig. 3. Synchronization timescale (T_{sync} , upper panel) and BH spin magnitude (χ_2 , bottom panel) as functions of central helium abundance. Three He star models are considered: a zero-age helium main sequence (He-Zams) star (solid line), a star with 10% central helium depletion (dashed line), and one with 30% central helium depletion (dash-dotted line). All models assume solar metallicity ($Z = Z_{\odot}$) and an initial orbital period of 1.0 day. Results for initial orbital periods of 0.5 and 2.0 d yield similar trends and are not shown.

the spin-to-orbital period ratio of the He star generally increases over time for fast-rotating models. In the lower-left panel, we find that higher initial rotation rates ($0.3\text{--}0.9 \omega_{\text{crit}}$) lead to larger BH spins at early times, but the spin magnitudes later converge to a narrow range of $\chi_2 \sim 0.08\text{--}0.10$. The synchronized model yields a slightly lower final spin, $\chi_2 \sim 0.07$, while the initially non-rotating model shows minimal tidal spin-up. For systems with the same physical conditions but a shorter initial orbital period of 0.5 d (right panels), tidal coupling is stronger, causing the final BH spin magnitudes to converge to a nearly uniform value of $\chi_2 \sim 0.1$, regardless of the initial stellar rotation. Thus, in wider systems, the final BH spin retains some memory of the He star’s initial spin, whereas in tighter orbits with stronger tides, the initial spin becomes largely irrelevant.

3.1.3. Tidal efficiency on the BH companion mass

In general, a more massive BH companion typically shortens T_{sync} (see Eq.(4) in Qin et al. 2018), leading to efficient tidal spin-up of the He star. Qin et al. (2018) investigated the impact of the BH companion mass on the spin magnitude of the resulting BH, but considered only companion masses of 10 and 30 M_{\odot} . To investigate whether the BH mass significantly affects the final spin of the newly-formed BH, we model a 20 M_{\odot} He Zams star paired with BH masses in a wide range of 3.0, 25, and 40 M_{\odot} in an initial orbit of 1.0 d. Surprisingly, as shown in Figure 5, the BH spin magnitude χ_2 remains largely unaffected by the BH companion mass throughout the evolution. This indicates that, for He stars in such close binaries, tidal synchronization is

efficient enough that the impact of varying BH mass on the final BH spin is negligible.

3.1.4. Tidal efficiency on the progenitor He star mass

In addition to tidal interactions, wind mass loss from the He star plays a crucial role in shaping the spin of the resulting BH. More massive He stars generally experience stronger stellar winds, leading to greater angular momentum loss. To investigate this effect, we conduct binary evolution simulations for systems consisting of a fixed 20 M_{\odot} BH and He stars with initial masses ranging from 5 to 70 M_{\odot} . The initial orbital periods are sampled uniformly in logarithmic space between 0.4 and 1.5 d². All He stars are assumed to have solar metallicity ($Z = Z_{\odot}$) and to be initially synchronized with the orbit.

In the upper panel of Figure 6, for a given initial orbital period, the spin magnitude χ_2 of the BH formed at the time of central carbon depletion decreases with increasing initial He star mass. This trend arises because more massive He stars are subject to stronger stellar winds, leading to greater angular momentum loss. A similar dependence is shown when varying the initial orbital period: longer periods result in weaker tidal synchronization and, through inefficient tides, lowers the retained spin angular momentum. These results indicate that while tidal interactions can efficiently synchronize He stars in close binaries, wind-driven mass loss is the dominant factor governing the final BH spin magnitude.

Bavera et al. (2021) derived approximations for the spin of close BH–He binaries, specifically designed for rapid incorporation into population synthesis codes (e.g., Banerjee & Olejak 2024). Using updated prescriptions for stellar winds and tidal interactions, we fit the spin magnitude of the BH formed from the He-star progenitor as a function of BH mass for a given initial orbital period. The lower panel of Figure 6 shows that, across different initial periods, the spin magnitude χ_2 decreases systematically with increasing BH mass, following an approximately exponential trend:

$$\chi_2 \propto e^{-\alpha M_{\text{BH}_2}}, \quad 0 \leq \chi_2 \leq 1.0, \quad (11)$$

where α is the decay coefficient. With α fixed at 0.3, we provide an analytic approximation for the different initial orbital periods (see the legend for the corresponding expressions). This decline of χ_2 with BH mass highlights the dominant role of stellar winds in removing angular momentum from more massive He stars.

3.2. Angular momentum transport efficiency on the resulting BH spin magnitude

The Tayler–Spruit (TS) dynamo (Spruit 1999, 2002), driven by differential rotation in radiative layers, is considered a key mechanism for efficiently transporting angular momentum between a stellar core and its radiative envelope. Such transport plays a critical role in setting the spin magnitude of the BH formed from a hydrogen-rich massive progenitor star (Qin et al. 2019), although tidal interactions can also be important. Qin et al. (2023) further examined the TS dynamo in massive He stars, demonstrating that efficient angular momentum transport tends to enforce quasi-solid-body rotation.

² We adopt 0.4 d as the lower limit for the initial orbital period, since more massive He stars would undergo initial Roche-lobe overflow.

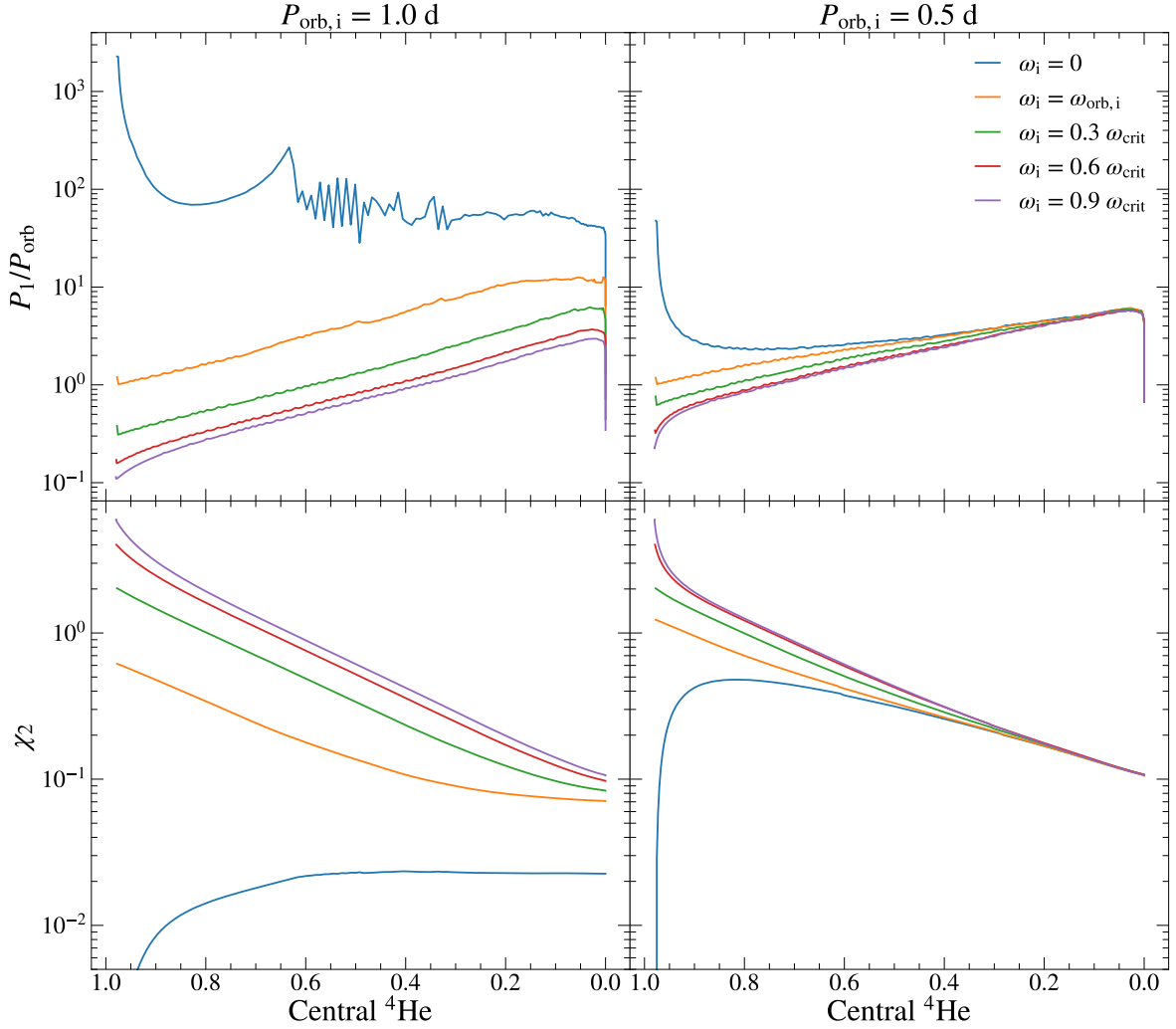


Fig. 4. Spin-to-orbital period ratio of the He star (*first row*) and the BH spin magnitude (*second row*) via direct core collapse as a function of its remaining central helium with varying initial rotation rates, $P_{\text{orb},i} = 1.0$ d (*left column*) and $P_{\text{orb},i} = 0.5$ d (*right column*). Different curves correspond to various initial rotation rates of the He star (blue: $\omega_i = 0$; orange: initially synchronized with the orbit; green: $\omega_i = 0.3 \omega_{\text{crit}}$; red: $\omega_i = 0.6 \omega_{\text{crit}}$; purple: $\omega_i = 0.9 \omega_{\text{crit}}$). The binary system consists of a $20 M_{\odot}$ BH and a $20 M_{\odot}$ He star.

The upper panel of Figure 7 shows the spin magnitude of BHs formed via the direct collapse of He stars at various evolutionary stages, for systems with an initial orbital period of $P_{\text{orb},i} = 1.0$ d and a $20 M_{\odot}$ BH companion. Different initial rotation rates are assumed for the He stars. The results indicate that the TS dynamo yields low-spin BHs (we assume the BH forms after the central carbon depletion), even when the progenitor He star begins with a high initial rotation rate. In the lower panel, we show that the total angular momentum retained in He stars at central carbon depletion differs by roughly an order of magnitude between models with and without the TS dynamo. Notably, the difference in spin magnitude and internal total angular momentum between models with and without the TS dynamo becomes negligible when He stars are assumed to be initially non-rotating, consistent with the findings of Bavera et al. (2020). In the following, we focus on models incorporating efficient angular momentum transport (i.e., TS dynamo) within He stars to explore the correlation between mass ratio q and inspiral effective spin χ_{eff} .

3.3. Correlation between mass ratio q and inspiral effective spin χ_{eff}

As demonstrated earlier, the BH spin magnitude is largely unaffected by the He star’s evolutionary stage at the onset of tidal interactions or the mass of its BH companion. However, mass loss due to stellar winds plays a dominant role, with more massive He star progenitors leading to lower-spin BHs. These findings underscore the efficiency of tidal synchronization in close BH-He binaries while highlighting the crucial impact of stellar winds on angular momentum evolution.

The effective inspiral spin, χ_{eff} , a key diagnostic for distinguishing among the formation channels of merging BBH systems (e.g., Abbott et al. 2016; Farr et al. 2017, 2018; Roulet et al. 2021), is defined as

$$\chi_{\text{eff}} = \frac{M_{\text{BH}_1} \vec{\chi}_1 + M_{\text{BH}_2} \vec{\chi}_2}{M_{\text{BH}_1} + M_{\text{BH}_2}} \hat{L}, \quad (12)$$

where M_{BH_1} and M_{BH_2} are the component BH masses, χ_1 and χ_2 are the corresponding dimensionless spin parameters, and \hat{L} is the direction of the orbital angular momentum.

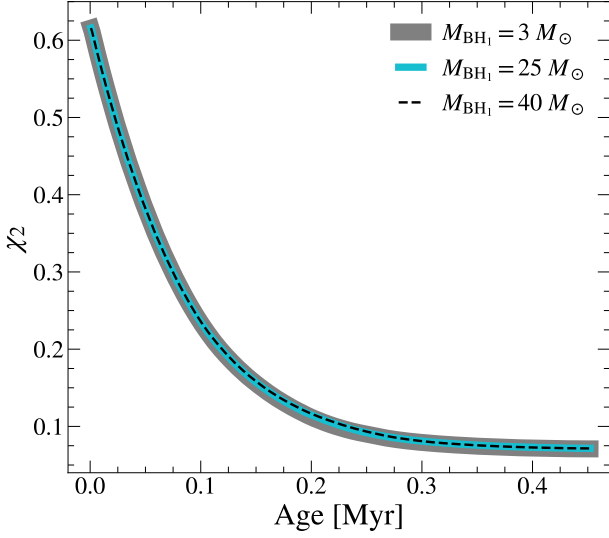


Fig. 5. The spin magnitude χ_2 of the BH, which forms through the direct core collapse of a He star, as a function of the stellar age. The binary system consists of a BH (gray solid line: $3 M_\odot$, cyan solid line: $25 M_\odot$, black dashed line: $40 M_\odot$) and a He star with an initial mass of $20 M_\odot$ in a 1.0-day orbit.

Given that the first-born BH typically has negligible spin ($\chi_1 \sim 0$; e.g., Figure 1 in Qin et al. 2018), the expression, under the assumption that χ_2 is aligned with the orbital angular momentum, reduces to

$$\chi_{\text{eff}} = \frac{q}{1+q} \chi_2, \quad (13)$$

where $q = M_{\text{BH}_2}/M_{\text{BH}_1}$ is the mass ratio of the binary system (hereafter, M_{BH_1} and M_{BH_2} denote the more massive and less massive BH, respectively).

Using the POWER-LAW+PEAK primary mass function and a POWER-LAW mass ratio distribution that are consistent with the results inferred by Abbott et al. (2023a), we randomly draw 10^5 pairs of black holes. We define the primary BH as the first-born BH with mass M_f , and the secondary BH as the second-born BH with mass M_s . Adopting the spin–mass relation of the secondary BH (Eq. 11, with an initial orbital period of $P_{\text{orb},i} = 0.40$ d), we investigate the relation between the mass ratio q and the effective inspiral spin χ_{eff} , as illustrated in the left panel of Figure 8. The figure compares the probability distribution of q and χ_{eff} for the observed BBH population (blue contours for the LIGO The LIGO Scientific Collaboration et al. 2025a) with that from our simulated systems (orange contours). Most observed BBHs cluster near equal masses and exhibit low, positive effective spins. Compared to the GWTC-3 results, the correlation between q and χ_{eff} in the updated population is less prevalent. Given the weak correlation, our predicted population is nevertheless consistent with the majority of observed systems exhibiting positive effective inspiral spin.

As a comparison, we switch the primary and secondary BH, as shown in the right panel. It predicts fewer systems in the region of low q and high χ_{eff} . We also examine this correlation for different initial orbital periods (see Figure A.1 in the appendix). We find that decreasing χ_{eff} is associated with increasing initial orbital period. In addition to the POWER-LAW+PEAK primary mass function, we also consider two alternative models: a uniform (Figure A.2) and a Gaussian distribution (Figure A.3). The correlation between q and χ_{eff} is sensitive to the choice of

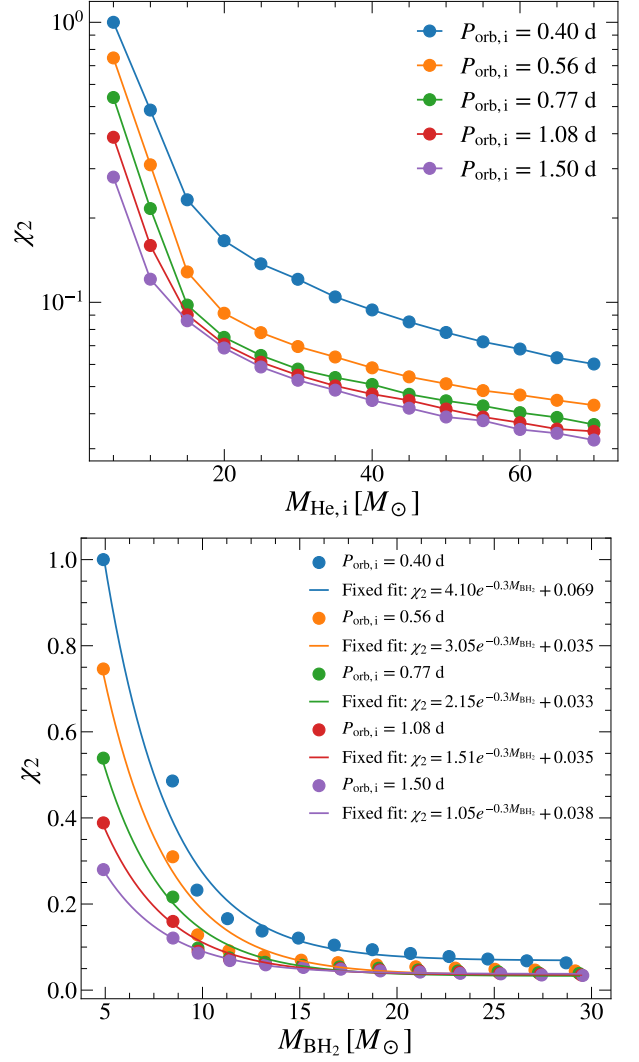


Fig. 6. Spin magnitude χ_2 of the BH, which forms via the direct core collapse of a He star at the central carbon depletion under the assumption of angular momentum conservation, with an initial mass from 5 to $70 M_\odot$ in increments of $5.0 M_\odot$, is shown as a function of the helium star's initial mass (upper panel) and of the resulting BH mass (lower panel). We consider a companion BH mass of $20 M_\odot$. Colored symbols represent different initial orbital periods: blue (0.40 d), orange (0.56 d), green (0.77 d), red (1.08 d), and purple (1.5 d). The solid lines represent the fitting data with a fixed exponent of $\alpha = 0.3$.

mass function, exhibiting notable differences from the POWER-LAW+PEAK case even when the initial orbital period is fixed.

4. Conclusions and discussion

As the final evolutionary stage prior to BH formation, He stars play a pivotal role in setting the resulting BH mass through their mass-loss history. Here, we model the evolution of massive He stars using the physically motivated wind prescription of Sander & Vink (2020), together with the revised, temperature-dependent formulation of Sander et al. (2023). In comparison with the standard Dutch wind scheme, commonly adopted in stellar evolution studies, the new prescription predicts significantly reduced mass loss.

Using the new wind prescription, we further examine key factors that may influence the spin magnitude of a BH inherited from its progenitor He star at solar metallicity in close binaries.

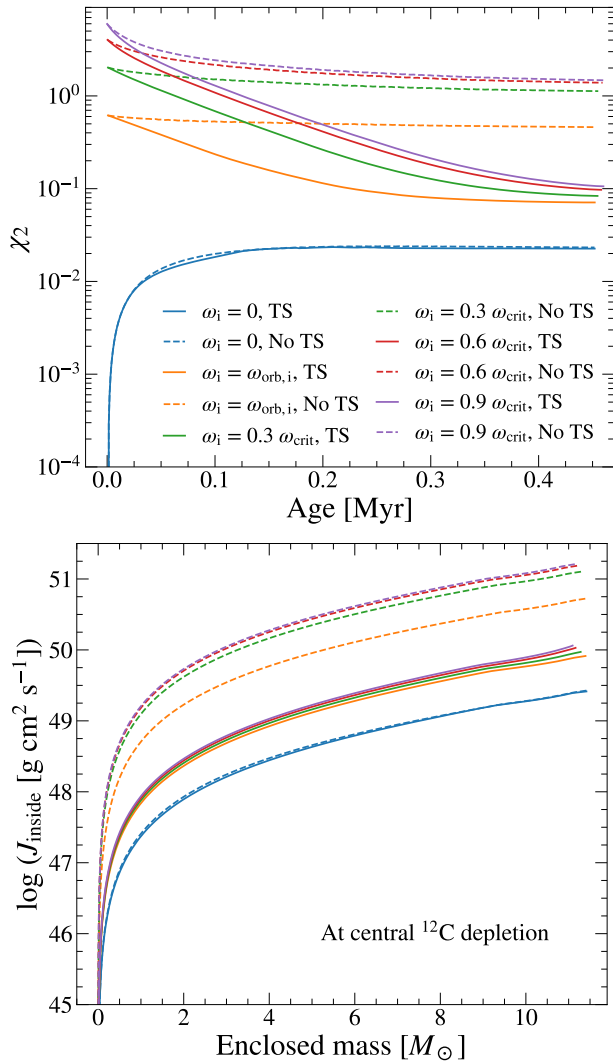


Fig. 7. *Upper panel:* same as Figure 5, but for a binary with a $20 M_{\odot}$ BH companion. Solid (dashed) lines denote models with (without) the TS dynamo. Lines with different colors correspond to various He star’s initial rotation rates (blue: $\omega_i = 0$; orange: initially synchronized with the orbit; green: $\omega_i = 0.3 \omega_{\text{crit}}$; red: $\omega_i = 0.6 \omega_{\text{crit}}$; purple: $\omega_i = 0.9 \omega_{\text{crit}}$). *Lower panel:* total internal angular momentum as a function of mass coordinate within the corresponding models at carbon depletion.

Our results show that the final spin is insensitive to both the evolutionary stage of the He star at the onset of tidal interactions and the mass of its companion. Moreover, the initial rotation of He stars has only a minor impact—particularly under strong tidal coupling—supporting the common assumption of initial orbital synchronization adopted in many studies. For different initial orbital periods, we find that the spin magnitude systematically decreases with increasing BH mass, approximately following an exponential trend. However, the efficiency of angular momentum transport within massive He stars can substantially modify this outcome, significantly influencing the spin magnitude of the resulting BH.

Adopting the POWER-LAW+PEAK primary mass function and a POWER-LAW mass ratio distribution that are consistent with the results inferred by Abbott et al. (2023a), we randomly draw 10^5 pairs of black holes, and assign χ_{eff} values to each system using the mass–spin relation (see Eq. 11). As shown in Figure 8, our simulated population remains broadly consistent, within current

uncertainties, with most GWTC-4.0 events that display positive effective inspiral spin in the q – χ_{eff} correlation (The LIGO Scientific Collaboration et al. 2025a). As alternatives, we also consider a uniform and a Gaussian primary mass distribution, and find that the q – χ_{eff} correlation is highly sensitive to the assumed mass function.

Predicting the properties of BBHs remains challenging owing to uncertainties in the physics of massive star evolution, both in isolation and in binaries (Belczynski et al. 2022). Recent models suggested that He stars may preserve a thin hydrogen layer on their surfaces after the common-envelope phase (Nie et al. 2025). Such an envelope can induce stellar expansion and trigger stable Case BB mass transfer onto the companion (Tauris et al. 2015; Qin et al. 2024b), thereby causing further mass and angular momentum loss of the BH progenitor. Another major uncertainty concerns whether BHs receive natal kicks at birth. In the isolated binary scenario, BH spins are generally expected to align with the orbital angular momentum (Kalogera 2000; Farr et al. 2017); however, strong natal kicks would be inconsistent with observations of Galactic BH binaries (e.g., Mandel 2016). BBH events with negative effective spins require at least one misaligned spin component, most likely induced by supernova kicks. Tauris (2022) showed that isolated binary evolution can still reproduce the observed BBH population if the BH spin axis is tossed during its formation in the core collapse of a massive star. Moreover, Baibhav & Kalogera (2024) explored various physical mechanisms that can affect both the BH spin magnitudes and spin–orbit misalignments.

The diversity of the observed BBH population suggests that multiple formation channels are at play, rather than a single one (e.g., Zevin et al. 2021; Mandel & Broekgaarden 2022; Cheng et al. 2023; Afroz & Mukherjee 2025; Colloms et al. 2025). For example, GW190517, which exhibits the largest measured χ_{eff} , has been suggested to arise from chemically homogeneous evolution (Qin et al. 2022), whereas GW191109, with the largest negative χ_{eff} , has been linked to a dynamical formation pathway (Zhang et al. 2023). More recently, the LVK Collaboration reported the BBH merger GW231123, with a total mass of 190 – $265 M_{\odot}$, whose formation channel remains uncertain (The LIGO Scientific Collaboration et al. 2025c).

Acknowledgements. Y.Q. acknowledges support from Anhui Provincial Natural Science Foundation (grant No. 2308085MA29) and the National Natural Science Foundation of China (grant Nos. 12473036 and 12573045). This work was partially supported by the Jiangxi Provincial Natural Science Foundation (grant Nos. 20242BAB26012 and 20224ACB211001) and by Anhui Province Graduate Education Quality Engineering Project (grant No. 2024qyw/sysfkc012). G.M. has received funding from the European Research Council (ERC) under the European Union’s Horizon 2020 research and innovation program (grant agreement No 833925, project STAREX). H.F. Song is supported by the National Natural Science Foundation of China (grant Nos. 12173010 and 12573034). All figures are made with the free Python module Matplotlib (Hunter 2007).

References

- Abbott, B. P., Abbott, R., Abbott, T. D., et al. 2016, *ApJ*, 818, L22
- Abbott, R., Abbott, T. D., Abraham, S., et al. 2021a, *Physical Review X*, 11, 021053
- Abbott, R., Abbott, T. D., Abraham, S., et al. 2021b, *ApJ*, 913, L7
- Abbott, R., Abbott, T. D., Acernese, F., et al. 2023a, *Physical Review X*, 13, 041039
- Abbott, R., Abbott, T. D., Acernese, F., et al. 2023b, *Physical Review X*, 13, 011048
- Acernese, F., Agathos, M., Agatsuma, K., et al. 2015, *Classical and Quantum Gravity*, 32, 024001
- Adamcewicz, C., Lasky, P. D., & Thrane, E. 2023, *ApJ*, 958, 13
- Adamcewicz, C. & Thrane, E. 2022, *MNRAS*, 517, 3928
- Afroz, S. & Mukherjee, S. 2025, *Phys. Rev. D*, 112, 023531

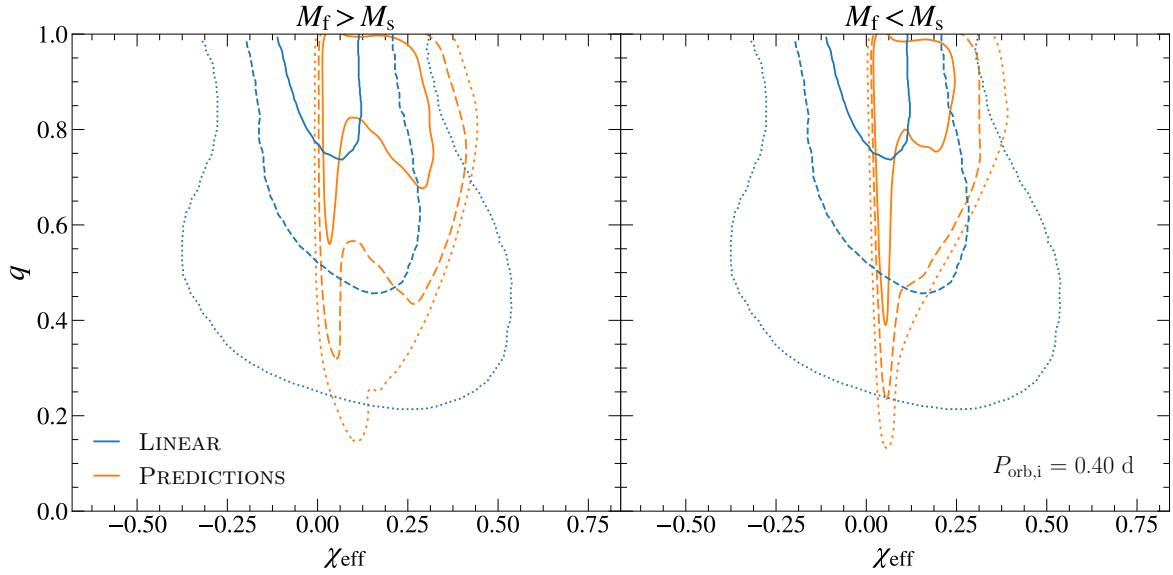


Fig. 8. Probability distributions of q versus χ_{eff} for 10^5 simulated BBHs are shown as orange contours (*left*: $M_f > M_s$, *right*: $M_f < M_s$). For comparison, blue contours indicate the population predictive distribution under the LINEAR model from The LIGO Scientific Collaboration et al. (2025a). Contours correspond to the 50%, 90%, and 99% credible intervals. The spin–mass relation of the secondary BH follows Eq. 11, assuming an initial orbital period $P_{\text{orb},i} = 0.40$ d.

- Akutsu, T., Ando, M., Arai, K., et al. 2021, *Progress of Theoretical and Experimental Physics*, 2021, 05A101
- Asplund, M., Grevesse, N., Sauval, A. J., & Scott, P. 2009, *ARA&A*, 47, 481
- Baibhav, V. & Kalogera, V. 2024, arXiv e-prints, arXiv:2412.03461
- Banerjee, S. & Olejak, A. 2024, arXiv e-prints, arXiv:2411.15112
- Bavera, S. S., Fragos, T., Qin, Y., et al. 2020, *A&A*, 635, A97
- Bavera, S. S., Zevin, M., & Fragos, T. 2021, *Research Notes of the American Astronomical Society*, 5, 127
- Belczynski, K., Holz, D. E., Bulik, T., & O’Shaughnessy, R. 2016, *Nature*, 534, 512
- Belczynski, K., Klencki, J., Fields, C. E., et al. 2020, *A&A*, 636, A104
- Belczynski, K., Romagnolo, A., Olejak, A., et al. 2022, *ApJ*, 925, 69
- Belczynski, K., Taam, R. E., Rantsiou, E., & van der Sluys, M. 2008, *ApJ*, 682, 474
- Böhm-Vitense, E. 1958, *ZAp*, 46, 108
- Broekgaarden, F. S., Stevenson, S., & Thrane, E. 2022, *ApJ*, 938, 45
- Brott, I., de Mink, S. E., Cantiello, M., et al. 2011, *A&A*, 530, A115
- Callister, T. A., Haster, C.-J., Ng, K. K. Y., Vitale, S., & Farr, W. M. 2021, *ApJ*, 922, L5
- Chaboyer, B. & Zahn, J. P. 1992, *A&A*, 253, 173
- Cheng, A. Q., Zevin, M., & Vitale, S. 2023, *ApJ*, 955, 127
- Colloms, S., Berry, C. P. L., Veitch, J., & Zevin, M. 2025, *ApJ*, 988, 189
- Cook, H. E., McKernan, B., Ford, K. E. S., et al. 2024, arXiv e-prints, arXiv:2411.10590
- de Jager, C., Nieuwenhuijzen, H., & van der Hucht, K. A. 1988, *A&AS*, 72, 259
- Delfavero, V., Ford, K. E. S., McKernan, B., et al. 2025, *ApJ*, 989, 67
- Eldridge, J. J. & Stanway, E. R. 2016, *MNRAS*, 462, 3302
- Farr, B., Holz, D. E., & Farr, W. M. 2018, *ApJ*, 854, L9
- Farr, W. M., Stevenson, S., Miller, M. C., et al. 2017, *Nature*, 548, 426
- Fragos, T., Andrews, J. J., Bavera, S. S., et al. 2023, *ApJS*, 264, 45
- Fuller, J. & Ma, L. 2019, *ApJ*, 881, L1
- Heger, A. & Langer, N. 1998, *A&A*, 334, 210
- Heger, A. & Langer, N. 2000, *ApJ*, 544 [arXiv:astro-ph/0005110]
- Higgins, E. R., Sander, A. A. C., Vink, J. S., & Hirschi, R. 2021, *MNRAS*, 505, 4874
- Hunter, J. D. 2007, *Computing in Science and Engineering*, 9, 90
- Hurley, J. R., Tout, C. A., & Pols, O. R. 2002, *MNRAS*, 329, 897
- Hut, P. 1981, *A&A*, 99, 126
- Jermyn, A. S., Bauer, E. B., Schwab, J., et al. 2023, *ApJS*, 265, 15
- Kalogera, V. 2000, *ApJ*, 541, 319
- Kruckow, M. U., Tauris, T. M., Langer, N., Kramer, M., & Izzard, R. G. 2018, *MNRAS*, 481, 1908
- Langer, N. 1998, *A&A*, 329, 551
- Langer, N., Fricke, K. J., & Sugimoto, D. 1983, *A&A*, 126, 207
- Li, Y.-J., Wang, Y.-Z., Tang, S.-P., Chen, T., & Fan, Y.-Z. 2025, *ApJ*, 987, 65
- Lyu, F., Yuan, L., Wu, D. H., et al. 2023, *MNRAS*, 525, 4321
- Maeder, A. & Meynet, G. 2000, *A&A*, 361, 159
- Mandel, I. 2016, *MNRAS*, 456, 578
- Mandel, I. & Broekgaarden, F. S. 2022, *Living Reviews in Relativity*, 25, 1
- Mapelli, M., Giacobbo, N., Santoliquido, F., & Artale, M. C. 2019, *MNRAS*, 487, 2
- Marchant, P., Renzo, M., Farmer, R., et al. 2019, *ApJ*, 882, 36
- McKernan, B., Ford, K. E. S., Callister, T., et al. 2022, *MNRAS*, 514, 3886
- Nie, Y.-D., Shao, Y., He, J.-G., et al. 2025, *ApJ*, 979, 112
- Nugis, T. & Lamers, H. J. G. L. M. 2000, *A&A*, 360, 227
- Olejak, A., Klencki, J., Xu, X.-T., et al. 2024, *A&A*, 689, A305
- Paxton, B., Bildsten, L., Dotter, A., et al. 2011, *ApJS*, 192, 3
- Paxton, B., Cantiello, M., Arras, P., et al. 2013, *ApJS*, 208, 4
- Paxton, B., Marchant, P., Schwab, J., et al. 2015, *ApJS*, 220, 15
- Paxton, B., Schwab, J., Bauer, E. B., et al. 2018, *ApJS*, 234, 34
- Paxton, B., Smolec, R., Schwab, J., et al. 2019, *ApJS*, 243, 10
- Peters, P. C. 1964, *Physical Review*, 136, 1224
- Qin, Y., Fragos, T., Meynet, G., et al. 2018, *A&A*, 616, A28
- Qin, Y., Hu, R. C., Meynet, G., et al. 2023, *A&A*, 671, A62
- Qin, Y., Marchant, P., Fragos, T., Meynet, G., & Kalogera, V. 2019, *ApJ*, 870, L18
- Qin, Y., Wang, Y.-Z., Bavera, S. S., et al. 2022, *ApJ*, 941, 179
- Qin, Y., Wang, Z.-H.-T., Meynet, G., et al. 2024a, *A&A*, 691, L19
- Qin, Y., Zhu, J.-P., Meynet, G., et al. 2024b, *A&A*, 691, A214
- Roulet, J., Chia, H. S., Olsen, S., et al. 2021, *Phys. Rev. D*, 104, 083010
- Roulet, J., Venumadhav, T., Zackay, B., Dai, L., & Zaldarriaga, M. 2020, *Phys. Rev. D*, 102, 123022
- Sander, A. A. C., Lefever, R. R., Poniowski, L. G., et al. 2023, *A&A*, 670, A83
- Sander, A. A. C. & Vink, J. S. 2020, *MNRAS*, 499, 873
- Santini, A., Gerosa, D., Cotesta, R., & Berti, E. 2023, *Phys. Rev. D*, 108, 083033
- Sciarini, L., Ekström, S., Eggenberger, P., et al. 2024, *A&A*, 681, L1
- Spera, M., Mapelli, M., Giacobbo, N., et al. 2019, *MNRAS*, 485, 889
- Spruit, H. C. 1999, *A&A*, 349, 189
- Spruit, H. C. 2002, *A&A*, 381, 923
- Stevenson, S., Vigna-Gómez, A., Mandel, I., et al. 2017, *Nature Communications*, 8, 14906
- Tauris, T. M. 2022, *ApJ*, 938, 66
- Tauris, T. M., Langer, N., & Podsiadlowski, P. 2015, *MNRAS*, 451, 2123
- The LIGO Scientific Collaboration, the Virgo Collaboration, & the KAGRA Collaboration. 2025a, arXiv e-prints, arXiv:2508.18083
- The LIGO Scientific Collaboration, the Virgo Collaboration, & the KAGRA Collaboration. 2025b, arXiv e-prints, arXiv:2508.18082
- The LIGO Scientific Collaboration, the Virgo Collaboration, the KAGRA Collaboration, et al. 2025c, arXiv e-prints, arXiv:2507.08219
- Vink, J. S. 2017, *A&A*, 607, L8
- Vink, J. S., de Koter, A., & Lamers, H. J. G. L. M. 2001, *A&A*, 369, 574
- Woosley, S. E. 2019, *ApJ*, 878, 49
- Woosley, S. E., Sukhbold, T., & Janka, H. T. 2020, *ApJ*, 896, 56
- Yoon, S.-C. 2017, *MNRAS*, 470, 3970
- Zahn, J. P. 1977, *A&A*, 57, 383
- Zevin, M. & Bavera, S. S. 2022, *ApJ*, 933, 86
- Zevin, M., Bavera, S. S., Berry, C. P. L., et al. 2021, *ApJ*, 910, 152
- Zhang, R. C., Fragione, G., Kimball, C., & Kalogera, V. 2023, *ApJ*, 954, 23

Appendix A: Supplementary Plots of q – χ_{eff} Correlation

Similar to Figure 8, Figure A.1 presents the two-dimensional probability distributions of q versus χ_{eff} for simulated BBHs with different initial orbital periods (*first row*: $P_{\text{orb},i} = 0.56$ d; *second row*: $P_{\text{orb},i} = 0.77$ d; *third row*: $P_{\text{orb},i} = 1.08$ d; *fourth row*: $P_{\text{orb},i} = 1.50$ d). For the shortest initial period ($P_{\text{orb},i} = 0.40$ d), Figures A.2 and A.3 show the corresponding distributions when adopting a uniform and a Gaussian primary BH mass function, respectively.

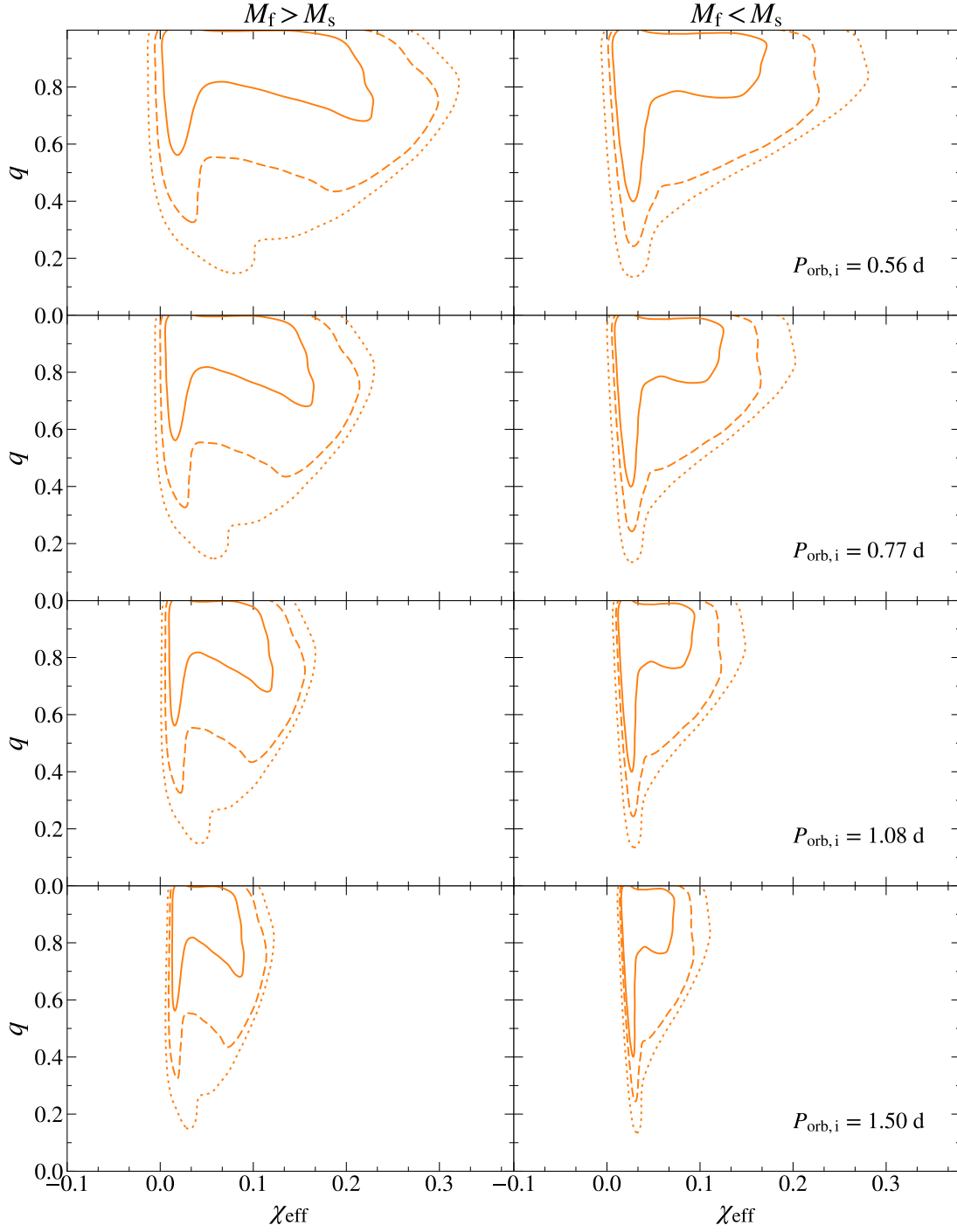


Fig. A.1. Same as Figure 8, but with the initial orbital period $P_{\text{orb},i} = 0.56$ d (first row), 0.77 d (second row), 1.08 d (third row), and 1.50 d (fourth row).

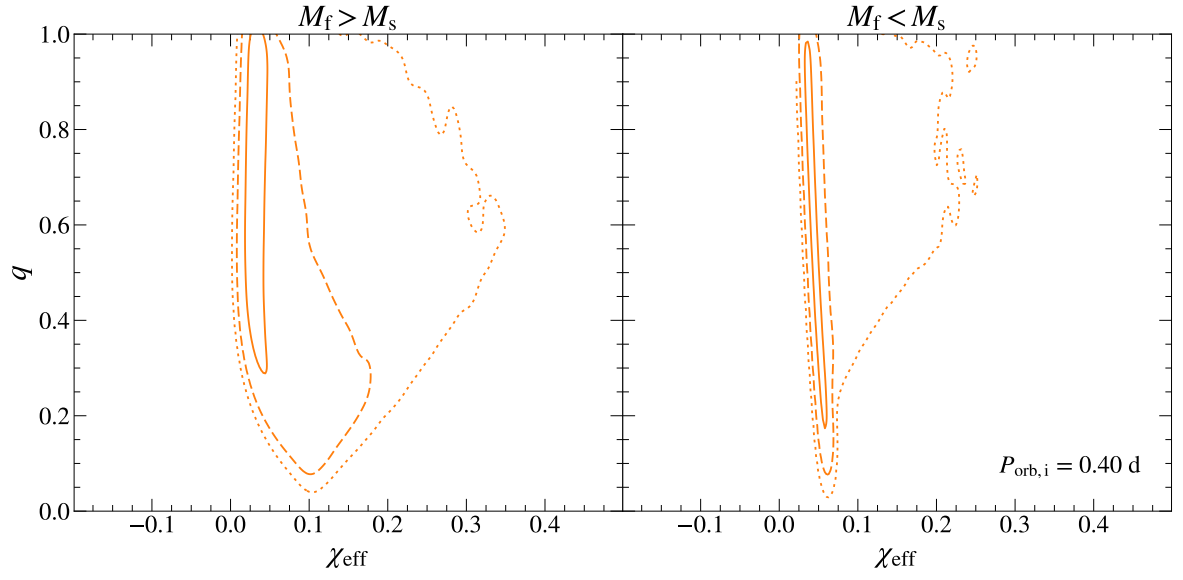


Fig. A.2. Same as Figure 8, but with primary mass function following uniform distribution from 5 to 45 M_{\odot} and the initial orbital period $P_{\text{orb},i} = 0.40$ d.

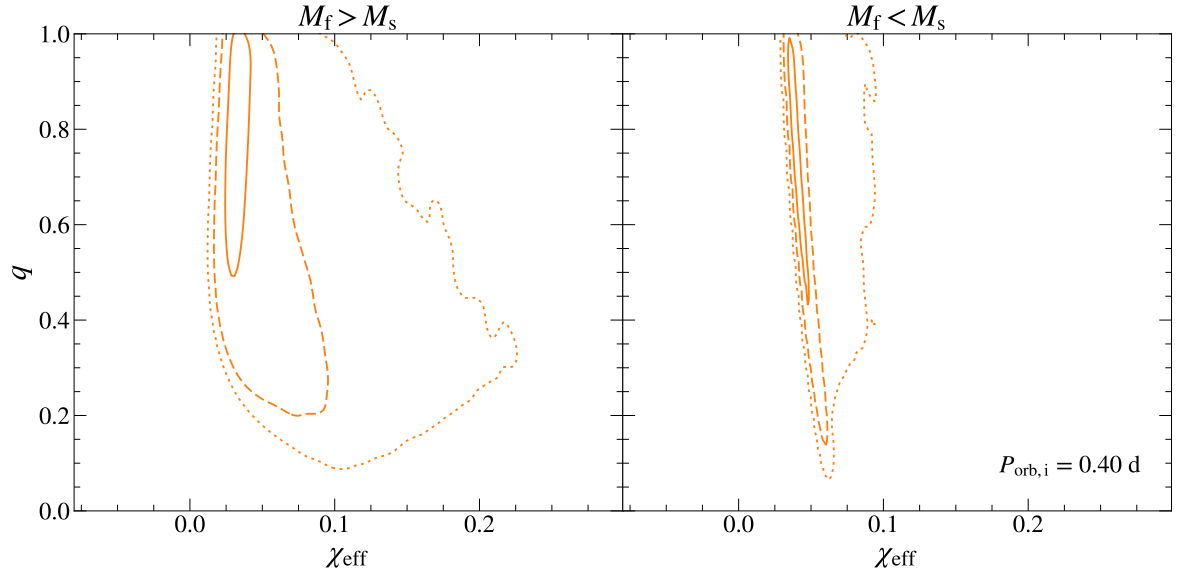


Fig. A.3. Same as Figure A.2, but with primary mass function following Gaussian distribution (mean = 25 M_{\odot} , standard deviation = 10 M_{\odot}).